

Anodic Shock-Triggered Exsolution of Metal Nanoparticles from Perovskite Oxide

Weiwei Fan, Baoming Wang, Rui Gao, Georgios Dimitrakopoulos, Jiayue Wang, Xianghui Xiao, Lu Ma, Kai Wu, Bilge Yildiz,* and Ju Li*



Cite This: *J. Am. Chem. Soc.* 2022, 144, 7657–7666



Read Online

ACCESS |



Metrics & More

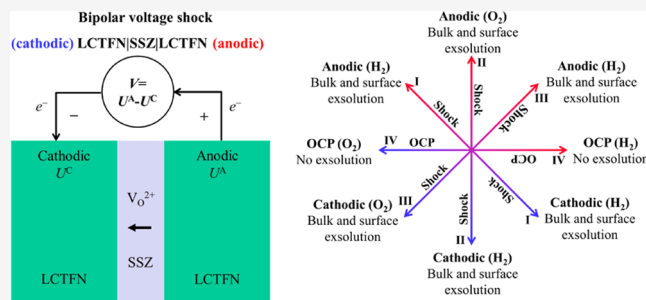


Article Recommendations



Supporting Information

ABSTRACT: Nanoparticles decorated electrodes (NDEs) are useful in fuel cells, electrolyzers, water treatment, and chemical synthesis. Here, we show that by rapidly bringing a mixed ionic-electronic conductor outside its electrochemical stability window, one can achieve uniform dispersion of metallic nanoparticles inside its bulk and at the surface and improve its electrocatalytic performance when back under normal functional conditions. Surprisingly, this can happen under anodic as well as cathodic current/voltage shocks in an ABO_3 perovskite oxide, $\text{La}_{0.4}\text{Ca}_{0.4}\text{Ti}_{0.88}\text{Fe}_{0.06}\text{Ni}_{0.06}\text{O}_{3-\delta}$ (LCTFN), across a wide range of H_2/O_2 gas environments at 800 °C. One possible mechanism for bulk Fe^0/Ni^0 precipitation under anodic shock condition is the incomplete oxygen oxidation ($\text{O}^{2-} \rightarrow \text{O}^{\alpha-}$, $0 < \alpha < 2$), migration and escape of oxygen to interfaces, and “whiplash” transition-metal reduction due to low electronic conductivity. We show that both cathodic and anodic shocks can produce NDEs to enhance electrocatalytic performance, potentially improving the flexibility of this approach in practical devices.



INTRODUCTION

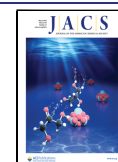
Solid oxide mixed ionic-electronic conductors (MIEC) are widely used in energy and chemical conversions. In particular, ABO_3 perovskite oxides¹ are versatile MIECs^{2–4} that have been used in high-temperature hydrogen fuel cells and water splitting.⁵ Exsolution, a technique whereby active transition metals in the host lattice precipitate out upon chemical or electrochemical reduction,⁶ has been used to form nanoparticle-decorated electrode (NDE) and shown to improve the electrocatalytic performance⁷ of perovskite oxide MIECs. Unlike catalysts produced through the wet impregnation method,^{8,9} NDEs prepared by in situ exsolution generally exhibit favorable thermal stability by virtue of the anchored morphologies of the nanoparticles (Figure S1).¹⁰ Here, we show that in addition to the reducing cathodic conditions (electrochemical potential $U \downarrow$ and electrons flowing into the MIEC), surprisingly, anodic shock ($U \uparrow$ and electrons flowing out of the MIEC) can also precipitate out metallic nanoparticles. Furthermore, both cathodic and anodic electrolytic shocks can produce NDEs with uniform bulk dispersion of metallic nanoprecipitates, as well as on the surfaces and grain boundaries. Electrochemical tests show enhanced performance when back to the normal range of U , either as a cathode or anode, due to the larger active electrocatalytic area of NDE for gas reactions.

Traditionally, exsolution was accomplished only in a chemically reducing atmosphere (i.e., high P_{H_2}) and was

time-consuming because of the sluggish diffusion and relatively low driving force ($\propto (k_B T)/2 \ln P_{\text{H}_2}$).^{11–14} However, if we apply external voltage U to shock the target perovskite lattice, there stands a good chance of realizing bulk and surface exsolution in a rapid manner over a wide atmospheric window, as shown by previous reports which applied electrochemical poling for the formation of NDEs.¹⁵ For a given ABO_3 perovskite oxide in a fixed atmospheric environment (P_{H_2} and P_{O_2}) and temperature T , an electrochemical stability window [U^{lower} , U^{upper}] should exist, like in the Pourbaix diagram, where operating the MIEC electrode within the window $U^{\text{lower}} < U < U^{\text{upper}}$ should maintain stability of the MIEC, and driving $U < U^{\text{lower}}$ (cathodic shock) or $U > U^{\text{upper}}$ (anodic shock) may cause reductive or oxidative phase transformation of the MIEC. It has been found that metal particles can be rapidly exsolved from oxide support through electrochemical poling.¹⁵ We naturally question what would happen if we drive an MIEC in the opposite high- U direction. Considering the good structural stability of Ti-based perovskites in a wide range of oxygen partial pressure, excellent

Received: December 9, 2021

Published: April 26, 2022



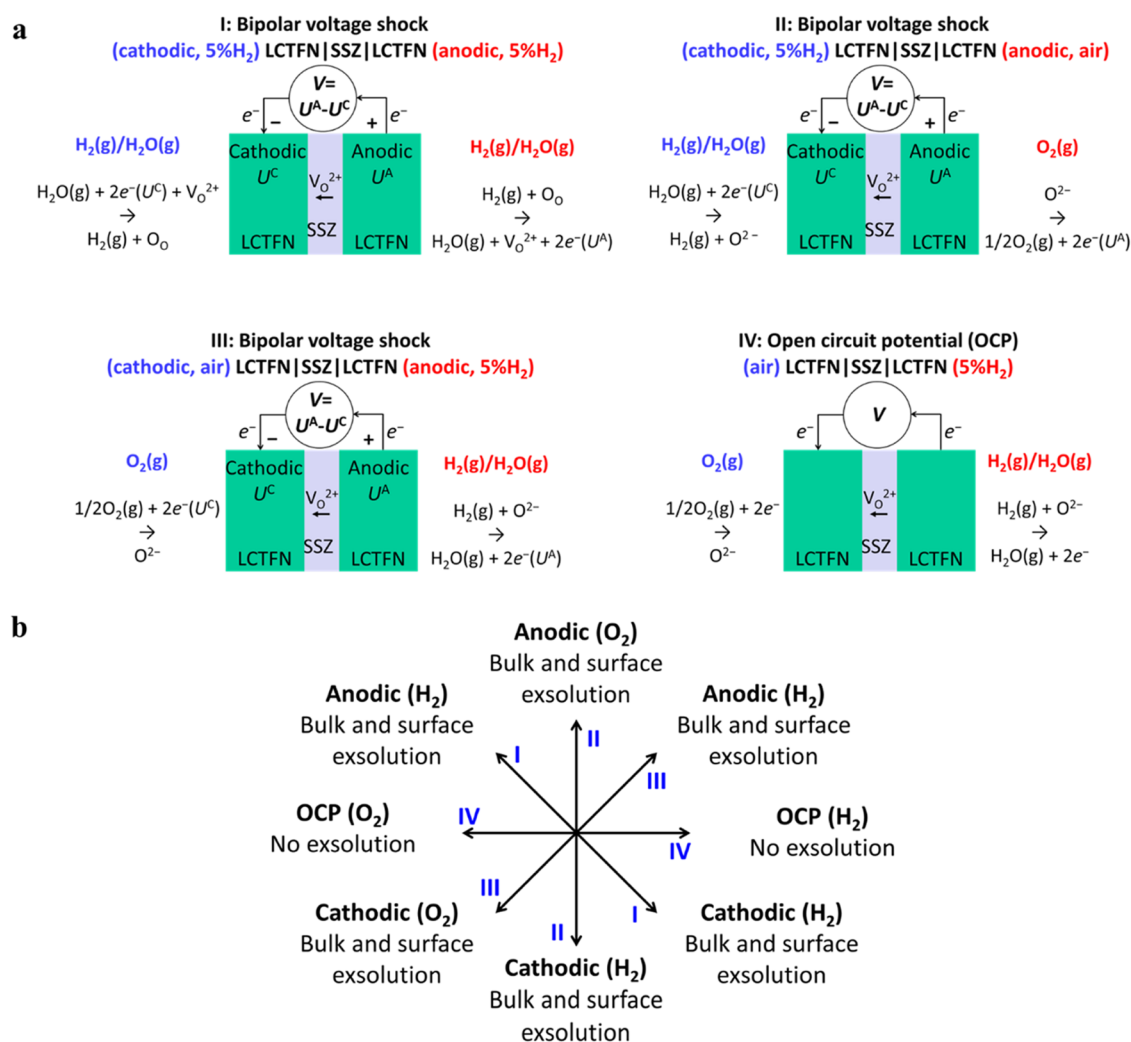


Figure 1. Cathodic and anodic shock-induced exsolution of nanoparticles from perovskite oxide. (a) Schematics of cell configuration and voltage shock modes (I, II, III, IV) performed under different polarities and atmospheres. (b) Quadrantal diagram of the resulting bulk and surface exsolution for LCTFN perovskite after voltage shock under different conditions.

catalytic activity of nickel and iron transition metals, and potential benefits of A-site deficiency on the exsolution, in this work, $\text{La}_{0.4}\text{Ca}_{0.4}\text{Ti}_{0.88}\text{Fe}_{0.06}\text{Ni}_{0.06}\text{O}_{3-\delta}$ (LCTFN) was designed and used as a model MIEC. When $U > U^{\text{upper}}$ and LCTFN starts to decompose, what product phases may we get? Addressing this question is not only of fundamental importance but may also expand the flexibility of the in situ NDE approach, as the LCTFN MIEC material may be used in a variety of operating modes, e.g., reversible fuel cell/electrolyzer and solid oxide co-electrolysis,^{16–18} where purely cathodic shock may not be practical *in operando*.

In this work, we demonstrate cathodic and anodic shock-triggered bulk and surface exsolution of metal nanoparticles from LCTFN perovskite using symmetrical cells under different atmospheres, four modes as depicted in Figure 1a. Here, for the first time, we show that not only cathodic (reducing) but also anodic (oxidizing) voltage shock produces a mass of nanoparticles emerging in the bulk as well as on the surface of the LCTFN (Figure 1b). As control, no bulk or surface exsolution was observed under open-circuit potential (OCP) in any of the atmospheres at the same temperature (800 °C).

RESULTS AND DISCUSSION

Voltage Shock-Induced Surface Exsolution from LCTFN Perovskite under Different Polarities and Atmospheres. To investigate the voltage shock-induced exsolution, $\text{Zr}_{0.89}\text{Sc}_{0.1}\text{Ce}_{0.01}\text{O}_{2-\delta}$ (SSZ) electrolyte-supported symmetrical cells with $\text{La}_{0.4}\text{Ca}_{0.4}\text{Ti}_{0.88}\text{Fe}_{0.06}\text{Ni}_{0.06}\text{O}_{3-\delta}$ (LCTFN) perovskite oxide (Figure S2 and Table S1) electrodes, LCTFN|SSZ|LCTFN (Figure S3), were adopted and first exposed in wet (~3% H₂O) 5% H₂/N₂ atmosphere under OCP. Subsequently, external electronic voltage (Figure S4) was applied across the cell using the homemade electrochemical cell setup (Figure S5). We have monitored the variation of the area-specific resistance by electrochemical impedance spectroscopy (EIS) under OCP after voltage shock (Figure S6, and also in Figure 4h), and we have deduced the onset voltage of particle exsolution from LCTFN perovskite when the impedance magnitude reduced sharply.

Under the open-circuit condition, after treatment in wet (~3% H₂O) 5% H₂/N₂ atmosphere for 100 h at 800 °C, a small number of particles (4 ± 1 particles μm^{-2}) with average size 96 ± 12 nm formed on the surface of LCTFN (Figure S7). TEM line-scan analysis verified that the exsolved particles were Ni⁰–Fe⁰ alloy (Figure S8). The reduction of NiO and Fe₂O₃ to

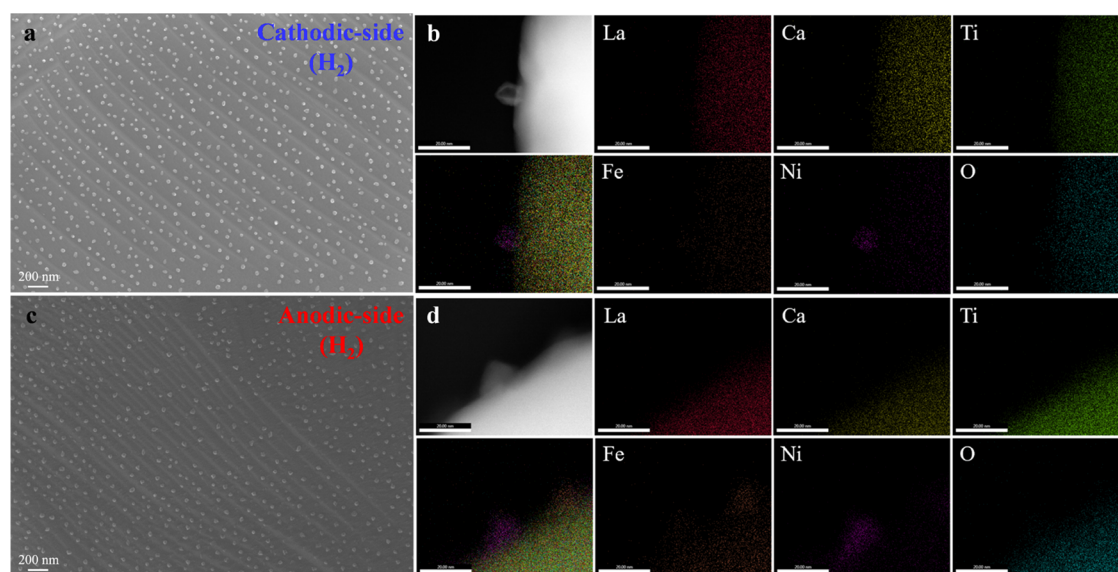


Figure 2. Surface exsolution characteristic of cathodic and anodic LCTFN of the cell (cathodic, 5% H_2) LCTFN/ISSZ/LCTFN (anodic, 5% H_2) after voltage shock. (a) SEM micrograph of the cathodic-side LCTFN after bipolar voltage shock to 3 V at 800 °C. (b) STEM-EDS mapping of exsolved nanoparticle on the surface of cathodic-side LCTFN (scale bar is 20 nm). (c) SEM micrograph of the anodic-side LCTFN. (d) STEM-EDS mapping of exsolved nanoparticle on the surface of anodic-side LCTFN (scale bar is 20 nm).

metallic Ni and Fe is thermodynamically favorable in H_2 at 800 °C due to the negative value of Gibbs free energy (Figure S9), whereas other metal oxides show positive Gibbs free energies (Table S2). The small density of metal particles can be justified by the relatively low driving force for phase decomposition and slow diffusion of metal cations at 800 °C. Regarding the large particle size, presumably, this was related with the A-cation (e.g., La)-rich surface, which hindered the particle nucleation. A rough estimation (the ratio of peak area/relative sensitivity) of the XPS data suggested an A-site surface enrichment (Table S3).

On the cell of mode I (cathodic, wet 5% H_2) LCTFN/ISSZ/LCTFN (anodic, wet 5% H_2), SEM showed that cathodic-side LCTFN presented a terrace-like structure (Figure 2a). Cathodic shock gave rise to the formation of well-dispersed nanoparticles with an average particle size of 24 ± 7 nm and a population density of 94 ± 27 particles μm^{-2} on the surface (Figure S10), which is much more populous compared to the OCP condition before. The formed metal nanoparticle precipitates out of a supporting oxide under cathodic conditions is consistent with previous reports.¹⁵ Nanoparticles prefer to nucleate at the terraces of the perovskite oxide surface (Figure S11). TEM-EDS revealed that the observed nanoparticles are Ni-rich (Figures 2b and S12). A lattice spacing of 0.206 nm was obtained (Figure S13), which is consistent with the (111) plane of the FCC Ni phase ($d_{\text{spacing}} = 0.204$ nm, PDF# 65-0380). Moreover, the exsolved nanoparticle socketed into the oxide support, forming a strong connection between the nanoparticle and the support.^{10,19}

Intriguingly, on the anodic-side LCTFN, too, a high density of zero-valent nanoparticles (average particle size 20 ± 8 nm and population density 68 ± 19 particles μm^{-2}) formed on the surface of the LCTFN (Figure 2c). Some of these nanoparticles were Ni-rich, while some were Fe-rich (Figures 2d and S14). XPS results further confirmed the existence of Fe^0 (Figures S15 and S16). According to the phase diagram of the binary Fe–Ni system, a solid solution of Fe–Ni with multiple atomic ratios can be easily formed because the elements are

adjacent in the periodic table.²⁰ Besides, it has been demonstrated that prior to the formation of Ni–Fe alloy, metallic Ni and Fe are generated first.²¹ HR-TEM results (Figure S17) showed that the observed nanoparticle was FeNi_3 intermetallic compound ($d_{\text{spacing}} = 0.251$ nm, 110 plane, PDF# 65-3244). XRD profiles revealed that the main perovskite structure remained after the voltage shock (Figure S18).

Additionally, our results showed that there was no significant variation in the particle size and population from the interface of electrolyte/electrode to the surface of the electrode (Figure S19). This relatively uniform distribution of particles across the electrode was probably related to the power uniformity (i.e., power per unit area) during voltage shock, which could affect the defect distribution of the oxide support as well as the exsolution. Indeed, in addition to the surface exsolution, bulk exsolution (shown in a later section) was also detected, indicating a strong driving force of the voltage shock. Thus, as compared to the gaseous atmospheric reduction (Figure S20), voltage shock could give rise to a rapid exsolution (several minutes) benefiting from the large driving force for decomposition created by the electrochemical potential (related to the equilibrium PO_2 on the Brouwer diagram and oxide off-stoichiometry in Gibbs free energy diagram), and accelerated diffusion of ions, consistent with prior reports.¹⁵ Moreover, the creation of oxygen vacancies under either cathodic or anodic shock conditions could provide potential sites for metal cluster nucleation.^{22,23} In sum, NDEs with small particle size and high population density were acquired in a short time on both the cathodic and anodic voltage shock sides of the cell in mode I. While this phenomenon has been observed under cathodic conditions earlier, the precipitation of metal nanoparticles under anodic conditions is intriguing and will be discussed later.

To further investigate the dependence of surface exsolution on electrode polarity as well as environmental atmosphere, the electrodes of symmetrical cells LCTFN/ISSZ/LCTFN were subjected to different gases using the homemade electrochemical cell setup (Figure S21).

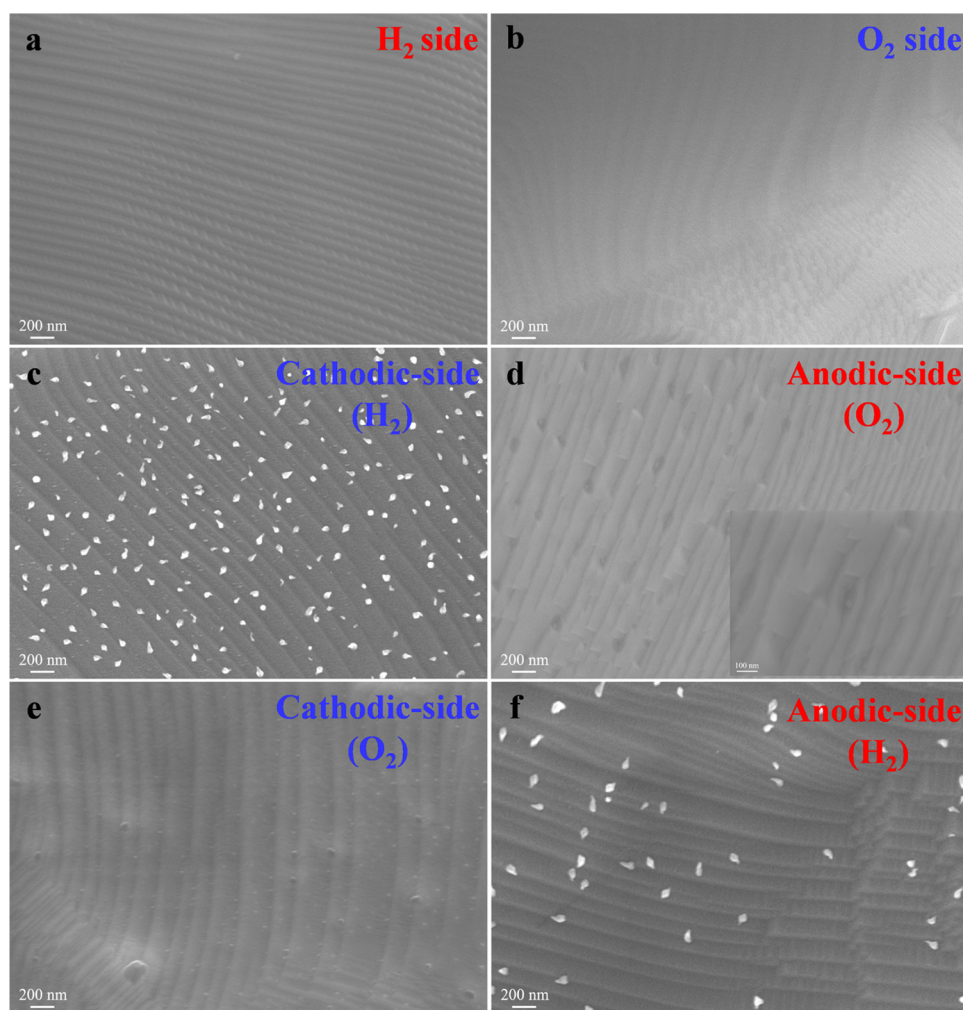


Figure 3. Surface exsolution characteristic of cells LCTFN/SSZ/LCTFN after treatment under different conditions. (a, b) SEM micrographs of H_2 and air sides of the cell (5% H_2) LCTFN/SSZ/LCTFN (air) after treatment at 800 °C for 2 h under OCP condition. (c, d) SEM micrographs of cathodic-side and anodic-side LCTFN of the cell (cathodic, 5% H_2) LCTFN/SSZ/LCTFN (anodic, air) after bipolar voltage shock to 5 V at 800 °C. (e, f) SEM micrographs of cathodic-side and anodic-side LCTFN of the cell (cathodic, air) LCTFN/SSZ/LCTFN (anodic, 5% H_2) after bipolar voltage shock to 5 V at 800 °C.

On the cell of mode IV, (air) LCTFN/SSZ/LCTFN (5% H_2), kept under OCP condition, no detectable surface exsolution occurred on either the hydrogen or the air sides (Figure 3a,b). This is due to the insufficient driving force for expelling metal from perovskite lattice. However, upon electrochemical polarization of the cell of mode II, (cathodic, wet 5% H_2) LCTFN/SSZ/LCTFN (anodic, air), numerous nanoparticles with an average particle size of 29 ± 10 nm and a population density of 27 ± 8 particles μm^{-2} (Figure S22) emerged on the cathodic-side surface (Figures 3c and S23–S25). The electrochemical driving force gave rise to the phase decomposition in a rapid manner. Moreover, similar to the case in wet H_2 , surface exsolution was also observed on the anodic side in air (average particle size 17 ± 3 nm and population density 3 ± 2 particles μm^{-2}) (Figures 3d and S26–S28), further demonstrating the possibility of exsolution from perovskite oxide under high anodic potentials.

In the cell of mode III, (anodic, wet 5% H_2) LCTFN/SSZ/LCTFN (cathodic, air), nanoparticles appeared on the surface of both the cathodic side (average particle size 15 ± 5 nm and population density 32 ± 9 particles μm^{-2}) in air and the anodic side (average particle size 42 ± 10 nm and population density

6 ± 5 particles μm^{-2} , Figure S29) in H_2 (Figures 3e,f and S30–S34). Even though the cathodic side is in air, the driving force supplied by electroreduction was stronger than that of gaseous oxidation by air; thus, the perovskite phase decomposition can still happen. Put in another way, the oxygen pumped out of the MIEC from its SSZ-contacting side (incentivized by the cathodic electronic current) exceeds surface reaction on the air-contacting side that may replenish some oxygen back to the MIEC, resulting in the precipitation of Fe^0/Ni^0 . Additionally, the main lattice structure was still maintained after the treatment (Figure S35).

Comparison to the control case at OCP (Figure 3a,b) showed that the gas reduction had a negligible contribution to the surface exsolution, while the voltage shock, both anodic and cathodic, could bring about surface exsolution, on both the air and the hydrogen sides (Table S4). To further investigate the gas agent effect on exsolution, the as-prepared symmetrical cell was also exposed to wet ($\sim 3\%$ H_2O) Ar, (cathodic, wet Ar) LCTFN/SSZ/LCTFN (anodic, wet Ar). Results showed that exsolution also took place on both cathodic and anodic sides after bipolar voltage shock to 3.5 V at 800 °C as the same routine of the other modes (Figure S36), further suggesting

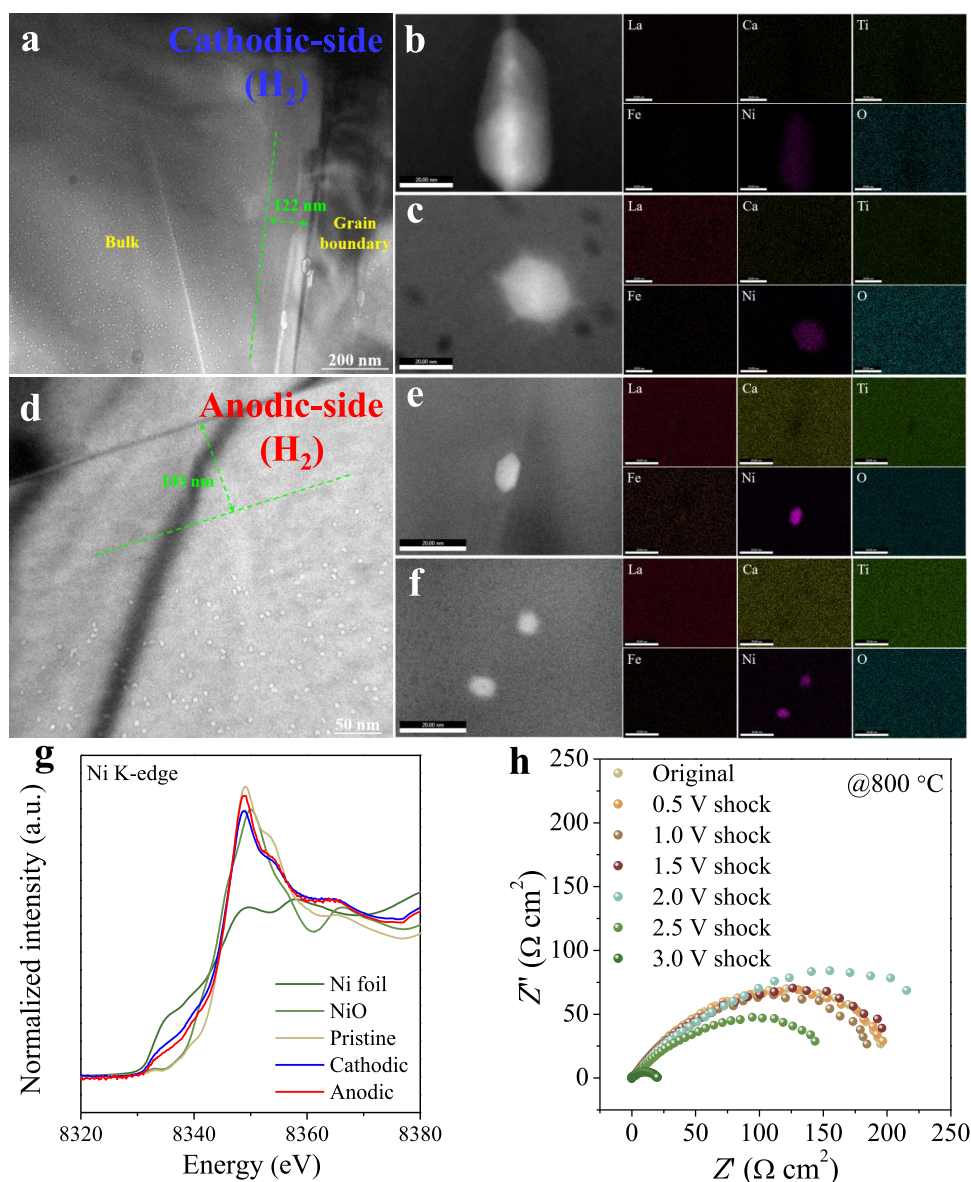


Figure 4. Bulk exsolution characteristic of cathodic and anodic LCTFN of the cell (cathodic, 5% H_2) LCTFN/SSZ/LCTFN (anodic, 5% H_2) after voltage shock. (a) TEM image of cathodic-side LCTFN after bipolar voltage shock to 3 V at 800 °C. The distance was measured by commercial software ImageJ. (b) STEM-EDS mapping of the nanoparticle exsolved at the grain boundary of cathodic-side LCTFN. (c) STEM-EDS mapping of the nanoparticle exsolved in the bulk of cathodic-side LCTFN. (d) TEM image of anodic-side LCTFN after bipolar voltage shock to 3 V at 800 °C. (e) STEM-EDS mapping of the nanoparticle exsolved at the grain boundary of anodic-side LCTFN. (f) STEM-EDS mapping of the nanoparticle exsolved in the bulk of anodic-side LCTFN. (g) Normalized Ni K-edge XANES collected from the cathodic and anodic sides. (h) Electrochemical impedance spectra of the cell (cathodic, 5% H_2) LCTFN/SSZ/LCTFN (anodic, 5% H_2) measured under OCP conditions before and after shocking at different voltages at 800 °C.

that the gas agent has negligible influence on the voltage shock-triggered exsolution. Besides, for different modes, it was observed that the shape and distribution of the exsolved particles were different. The difference in the shape was probably associated with the different adsorbed gas equilibria on the surface, resulting in a change in the surface energy of different facets of the particle.^{24–26} Generally, the equilibrium shape of the exsolved particle is closely related to the local facet geometry.²⁴ Thus, some shapes are preferable compared to others in minimizing their total free energy.²⁷ As to the difference of the distribution, presumably, this was related with the defects (such as oxygen vacancies)^{23,28} preexisting as well as additionally generated on the oxide support during voltage shock, which could be potential nucleation sites. Due to the

different driving forces supplied to each side of each mode, relating to the different atmosphere and potential, the distribution and number of the additionally formed defects on the surface of the oxide support should be different.

Voltage Shock-Induced Bulk Exsolution in LCTFN Perovskite under Different Polarities and Atmospheres.

Since the entire perovskite oxide could be treated during voltage shock, it is important to see if there are regional differences from surface to bulk. Hence, the focused ion beam (FIB) technique was applied to produce an LCTFN lamella with ~ 100 nm thickness (Figure S37), which was then characterized by TEM.

For the cell of mode IV at OCP, bulk exsolution took place on neither the hydrogen electrode nor the air electrode side

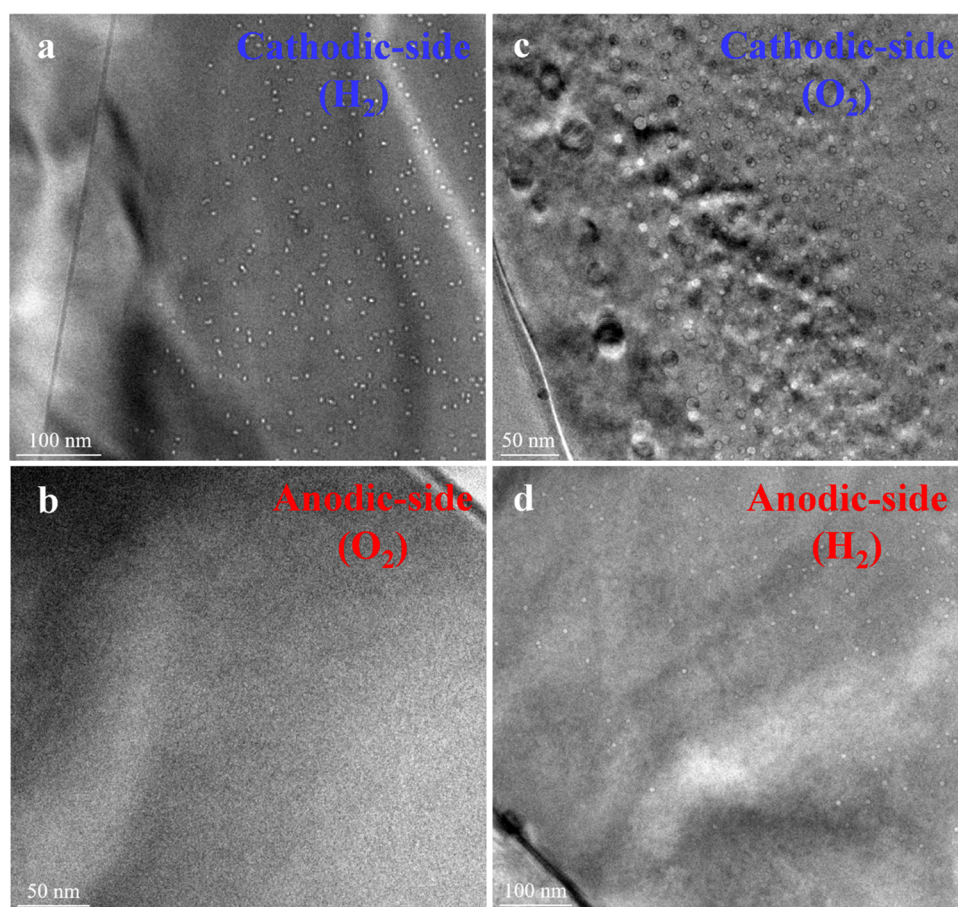


Figure 5. Bulk exsolution characteristic of cathodic and anodic LCTFN of the cells of modes II and III. (a, b) TEM images of cathodic and anodic LCTFN of the cell (cathodic, 5% H_2) LCTFN/SSZ/LCTFN (anodic, air) after bipolar voltage shock to 5 V at 800 °C. (c, d) TEM images of cathodic and anodic LCTFN of the cell (cathodic, air) LCTFN/SSZ/LCTFN (anodic, 5% H_2) after bipolar voltage shock to 5 V at 800 °C.

(Figure S38). However, upon electrochemical polarization of the cell of mode I, (cathodic, wet 5% H_2) LCTFN/SSZ/LCTFN (anodic, wet 5% H_2), a large number of nanoparticles emerged in the interior of the grains and along the grain boundaries (Figure 4a) of the cathodic side (average particle size 4 ± 1 nm). Considering the TEM result is a projection of 3D volume to a 2D surface along a certain Z direction, we could roughly convert the unit of particles μm^{-2} from the 2D surface (surface area $S = XY$, length X and width Y could be measured from the TEM image) to the unit of particles μm^{-3} as an estimation of the bulk population density by dividing the depth of the lamella. After using 100 nm (a rough thickness of the lamella) as the Z value, a bulk population density of $16\,000 \pm 4600$ particles μm^{-3} (Figure S39) was obtained for the cathodic side of mode I. However, no apparent nanoparticle could be observed in the region between the green dash line and the grain boundary. A denuded zone of ~ 122 nm was formed from the nearest GB. This zone was formed most probably due to the diffusion of exsolvable metal (M) cations to the adjacent grain boundary, leading to the M-depleted area. It has been reported in the literature that, to sustain exsolution on the surface, typically, reducible cations from ~ 100 nm depth diffuse to the surface and this also forms a denuded zone.¹⁰ This depth value is very close to our result. Additionally, we found that the bulk particles generally presented a smaller size (R) than that of the particles at the grain boundary and on the surface, $R_{\text{bulk}} < R_{\text{gb}} < R_{\text{surf}}$ following the relative diffusivities (D) of ions in bulk versus at extended

defects, as $D_{\text{bulk}} < D_{\text{gb}} < D_{\text{surf}}$. The grain boundary and surface commonly can offer a larger free volume, which favors the particle nucleation and growth, and thus generally gives rise to a larger particle size. In addition, this could be related to the strain associated with the particle growth since a smaller particle is usually easier to accommodate in the bulk of oxide support.²⁹ TEM-EDS results revealed that the particle appearing at the grain boundary was $\text{Ni}^0\text{--Fe}^0$ alloy (Figures 4b, S40, and S41), while the Ni signal was stronger than that of other elements for the bulk particle (Figures 4c, S42, and S43).

On the anodic side, too, of the cell in mode I (Figure 4d), a number of nanoparticles also appeared in the bulk (average particle size 3 ± 1 nm and bulk population density $17\,000 \pm 4700$ particles μm^{-3}). Similarly, a particle-free region of ~ 103 nm was also formed from the grain boundary after the voltage shock. TEM results confirmed the exsolution of Ni at the grain boundary and in the bulk of oxide support (Figures 4e,f and S44–S47). In addition, XANES results indicated the appearance of Ni^0 in both cathodic and anodic sides after voltage shock (Figure 4g). Moreover, quantitative analysis based on a linear combination fitting showed that 23% Ni^0 formed on the cathodic side, and the average oxidation state was about +1.54. For the anodic side, 13% Ni^0 was generated and the average oxidation state was around +1.74. Thus, prolific homogeneous nucleation of zero-valent nanoparticles can be achieved on both sides through a voltage shock (Figure S48). Benefiting from the nanoparticle exsolution, the cell impedance reduced remarkably after the voltage shock

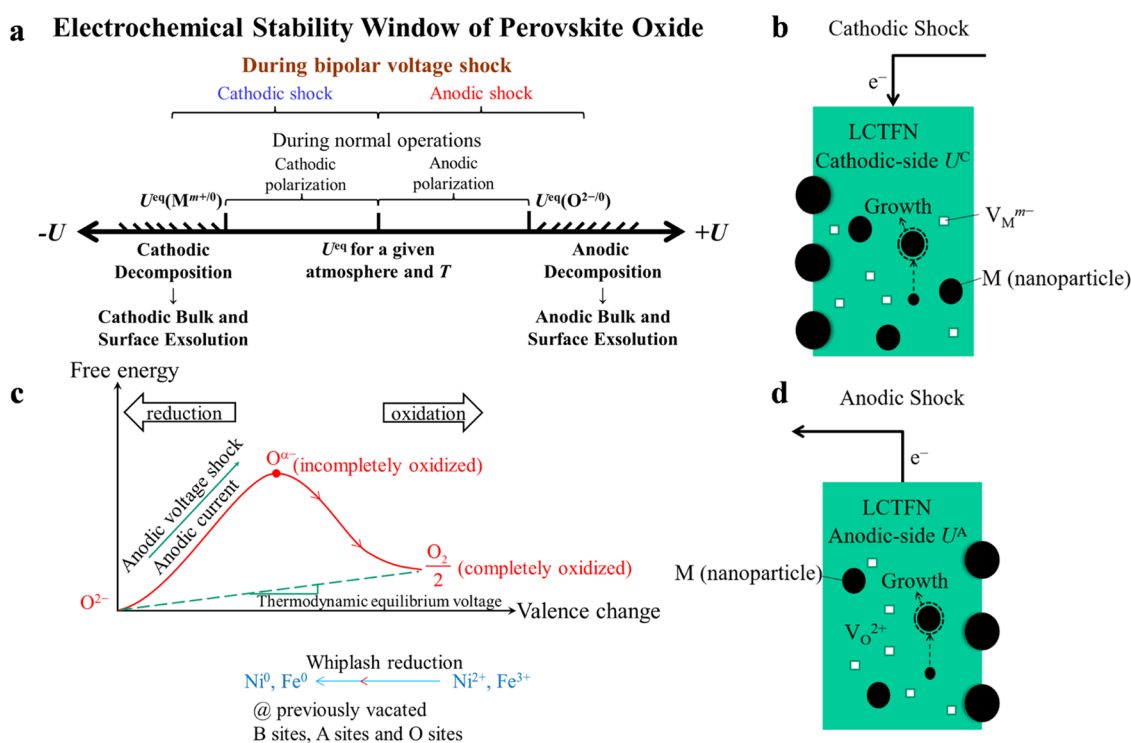


Figure 6. Illustration of voltage shock-induced exsolution. (a) Schematic of the electrochemical stability window of perovskite oxide. (b) Schematic of cathodic shock-induced bulk and surface exsolution during voltage shock. (c) Diagram of the “charge whiplash” effect. (d) Schematic of anodic shock-induced bulk and surface exsolution during voltage shock.

(Figures 4h and S49–S52), indicating much improved reactivity.

Upon electrochemical polarization of the cell in mode II, numerous nanoparticles emerged in the bulk of the cathodic side (particle size 3 ± 1 nm and bulk population density $14\,000 \pm 4100$ particles μm^{-3} , Figure S53) due to the enhanced reducing driving force (Figures 5a and S54–S57). Moreover, bulk exsolution was also detected on the anodic side (Figures 5b and S58). As for the cell of mode III, even in oxidizing atmosphere, a lot of nanoparticles formed in the bulk (particle size 5 ± 2 nm and bulk population density $21\,000 \pm 6100$ particles μm^{-3} , Figure S59) of the cathodic side (Figures 5c and S60–S62), further demonstrating the influx of electrons into the perovskite lattice and the sufficient reducing ability to cause the phase decomposition. Concurrently, bulk exsolution was also observed (particle size 4 ± 1 nm and bulk population density 9700 ± 2900 particles μm^{-3}) on the anodic side (Figures 5d and S63–S66). In summary, cathodic and anodic shock-induced bulk exsolution of nanoparticles from perovskite oxide could be obtained in a wide range of atmospheric conditions.

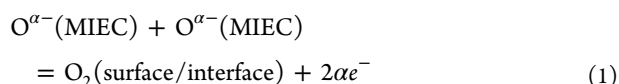
Mechanisms of Voltage Shock-Induced Exsolution. In principle, there should be an electrochemical stability window $U^{lower} < U < U^{upper}$ for a perovskite oxide $ABO_{3\pm\delta}$ at a given temperature, which is equivalent to a PO_2^{eq} or oxide off-stoichiometry window, assuming thermodynamic equilibrium between the gas phase and the solid-phase ionic/electronic disorders. Recall that on the standard Brouwer diagram for a single metal oxide phase, there is a one-to-one relation between PO_2^{eq} and the Fermi energy inside (electrode voltage U , thermodynamic potential of the electrons) that controls electron-to-hole concentration ratio $[e^-]/[h^*]$; PO_2 is also related to the chemical potential of oxygen,³⁰ μ_O ($\mu_O = \mu_O^0 +$

$RT \ln(PO_2)/2$), which can be found by tangent extrapolation of the Gibbs free energy curve with respect to the oxide composition X_O , which is related to the oxygen off-stoichiometry ratio δ .³¹ δ describes solid–gas equilibrium (essentially, amount of oxygen gas evolution/uptake), and the degree of the ionic disorder on the anion sublattice (i.e., oxygen vacancies) and the cation sublattice (i.e., metal interstitials) of the perovskite oxide, which also controls the electronic disorders (electrons/holes/polarons) that accompany the atomic imperfections in the oxide.^{31,32} Thus, U , PO_2^{eq} , μ_O , X_O , and δ have one-on-one relationship with each other, so long as a single solid phase (here, a random solid solution of $ABO_{3\pm\delta}$) is maintained within the stability window, phase decomposition would not take place. If sufficient electrochemical driving force is provided, the condition can go out of the electrochemical stability window of the random solid solution phase, and second phase formation can be thermodynamically expected under both cathodic and anodic conditions (Figure 6a). Under cathodic conditions, we believe the underlying mechanism is the extreme reduction of the perovskite oxide introduced by cathodic electrochemical potential. Under anodic voltage shock, we propose one potential mechanism: incomplete oxidation leading to oxygen evolution and charge transfer locally.

Cathodic Shock. During the cathodic shock, the influx of electrons into the perovskite lattice and outflux of oxygen anions through the electrolyte strongly drives and accelerates the reduction of the reducible metal cations and the creation of oxygen vacancies as well as Schottky defects²³ (Figure 6b). Thereafter, nucleation can preferentially take place on extended defects or point defects or point defect clusters.^{23,33} For example, Besenbacher et al. have found that Au clusters preferentially nucleate at oxygen vacancies on TiO_2 .²⁸ In

addition, in our recent work, Wang et al. have shown that oxygen vacancy clusters serve as nucleation sites for metal nanoparticle exsolution on a perovskite oxide, $\text{La}_{0.6}\text{Sr}_{0.4}\text{FeO}_3$.²³

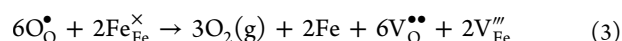
Anodic Shock. The observation that anodic voltage shock gives rise to metal nanoparticle precipitation out of a perovskite oxide is novel and intriguing. Here, we propose one possible mechanism called “charge whiplash” effect from the voltage shock (Figure 6c): that is, upon $+U$, some O^{2-} in the bulk is first oxidized into an incompletely oxidized form $\text{O}^{\alpha-}$ ($\alpha = 1$: peroxide; $\alpha = 0.5$: superoxide). The $\text{O}^{\alpha-}$ ($0 < \alpha < 2$) is much more mobile than O^{2-} . For example, it has been demonstrated that the diffusion energy barrier of O^{1-} is 0.9 eV, while it is 2.3–4.0 eV for O^{2-} in layered transition-metal oxides,^{34,35} and it will migrate and collect at free volumes like internal and external surfaces and interfaces. These $\text{O}^{\alpha-}$ species created by the out-of-equilibrium anodic voltage shock are highly unstable energetically and tend to undergo further spontaneous oxidation:



when they collect and meet each other, forming a charge-neutral O_2 molecule ($\alpha = 0$) at the surface or grain boundary free volumes, while leaving behind $2\alpha e^-$ (MIEC) free electrons as “excess negative charge”. If at thermodynamic equilibrium, these e^- (MIEC) should go to the current collector quasi-statically (by two-way exchange currents) as the metal electrode’s Fermi energy is pinned there by the external circuit as $-eU$. However, the MIEC is not necessarily a good electron conductor,^{36,37} and local electronic disorder may not reach global thermodynamic equilibrium, so the excess $2\alpha e^-$ (MIEC) in eq 1 may rather reduce Ni and Fe cations nearby, especially near the oxygen vacancies created by the aforementioned escaping oxygen.

To accentuate the interesting features of the “charge whiplash” inside MIEC polycrystal (3D), let us contrast them with the anodic oxygen evolution reaction (OER) occurring on Pt surfaces (2D) in the classic water-splitting experiment, where two H_2O molecules are oxidized completely to the O_2 molecule, leaving behind $4e^-$ (Pt). Note that Pt is an excellent electron conductor, but does not conduct oxygen, so there is no MIEC “charge whiplash” and the $4e^-$ (Pt) are promptly sucked out to the external circuit. In contrast, the reactions inside solid 3D MIEC undergoing an overall oxidation reaction could be more complicated due to the variable electronic and ionic conductivities. There can be “incomplete oxidation” of individual oxygen ion, where due to the rapid $U \uparrow$ and lack of opportunities to meet other $\text{O}^{\alpha-}$ and nucleation sites for forming O_2 , an out-of-thermodynamic equilibrium electron-transfer reaction $\text{O}^{2-} \rightarrow \text{O}^{\alpha-}$ ($0 < \alpha < 2$) may happen inside the lattice, where the $2-\alpha$ electrons are sucked into the metallic current collector, giving the overall anodic shock current (for example, $\alpha = 1$, eq 2). Unlike surface reactions on Pt surface, such incomplete oxidation reactions can happen plentifully inside the lattice interior of MIEC. However, as these peroxide and superoxide $\text{O}^{\alpha-}$ intermediates in the bulk lattice are less thermodynamically stable (compared to O_2) due to the voltage shock (see illustration in Figure 6c), and also much more mobile, over a somewhat longer timescale, these $\text{O}^{\alpha-}$ intermediates can spontaneously migrate hundreds of nanometers to interfaces for O_2 nucleation, as eq 1 shows, to complete the “incomplete oxidation”. Then and there, because

of the relatively poor electronic conductivity of MIEC, the remaining αe^- (MIEC) can reduce adjacent cations, causing a “whiplash reduction” of metal cations. Thus, MIEC-mediated charge transfer reactions can be much more delocalized than the Pt surface anode. Spatially, we have counteracting, internal whiplash charge currents inside the MIEC lattice (ionic current carried by the moving $\text{O}^{\alpha-}$ toward the GBs/surfaces, and electronic current αe^- (MIEC) moving in the opposite direction) that cancel internally, and thus do not contribute to the net anodic current overall, but they can cause consequential compositional changes in the interior of the MIEC anode (for example, $\alpha = 1$, $M = \text{Fe}$, eq 3). Similarly, cluster nucleation and particle growth would take place as exsolution progresses until reaching a new equilibrium (Figure 6d).



Put another way, it is well understood that any generic metal oxide MO phase can be electrolyzed into $\text{O}_2(\text{gas})$ and M^0 , if larger than thermodynamic equilibrium voltage (green dash line in Figure 6c) is supplied. In standard electrolyzer configuration, the M^0 and $\text{O}_2(\text{gas})$ products are separated by macroscopic distances, collected on two cleanly separated electrodes (anodic electrode collects $\text{O}_2(\text{gas})$ product and cathodic electrode collects M^0 product) connected by macroscopic metal wiring and an external power source. What we see under extreme anodic shock voltages (solid green arrow in Figure 6c) ~ 5 V, that likely far exceed the thermodynamic equilibrium voltage, is that even though the LCTFN MIEC is nominally an anode as a whole, there are also effectively internal microscopic cathodes distributed inside the body that give a plethora of M^0 electrolyzing products, separated only by microscopic distances away from the $\text{O}_2(\text{gas})$ electrolyzing products collected on surfaces and grain boundaries. The “metal wiring” in this context is replaced by not-so-good electronic conductivity of the MIEC body, and the “power source” is replaced by the excess free energy (difference between solid green and dash green lines in Figure 6c) stored in the form of $\text{O}^{\alpha-}$ ($0 < \alpha < 2$) species created by the shock overpotential. In this perspective, anodic shock-triggered exsolution of M^0 may also be understood as “internal electrolyzing of MO”.

CONCLUSIONS

Intriguingly, we have found that not only cathodic (as known in literature) but also anodic voltage shock leads to the formation of metal nanoparticles in the bulk and at the surface of a perovskite oxide under a wide range of atmospheres. The fact that this phenomenon takes place also under anodic electrochemical conditions is not trivial. One mechanism that can explain this phenomenon is incomplete oxidation leading to oxygen evolution and charge transfer locally, due to highly variable electronic conductivity of the perovskite. The ability to obtain rapid bulk and surface exsolution under both cathodic and anodic voltage conditions widens the window for use of exsolution-based nanoparticle catalysts in a range of electrochemical applications.

■ ASSOCIATED CONTENT

SI Supporting Information

The Supporting Information is available free of charge at <https://pubs.acs.org/doi/10.1021/jacs.1c12970>.

Experimental procedures, XRD profiles, schematic of setups, EIS data, TEM images, particle size distribution, XPS data, SEM images, additional discussions, refined parameters, thermodynamic data, and summary of particle density and population (Tables S1–S3) (PDF)

■ AUTHOR INFORMATION

Corresponding Authors

Bilge Yildiz – Department of Nuclear Science and Engineering, Massachusetts Institute of Technology, Cambridge, Massachusetts 02139, United States; Department of Materials Science and Engineering, Massachusetts Institute of Technology, Cambridge, Massachusetts 02139, United States; orcid.org/0000-0002-2688-5666; Email: byildiz@mit.edu

Ju Li – Department of Nuclear Science and Engineering, Massachusetts Institute of Technology, Cambridge, Massachusetts 02139, United States; Department of Materials Science and Engineering, Massachusetts Institute of Technology, Cambridge, Massachusetts 02139, United States; orcid.org/0000-0002-7841-8058; Email: liju@mit.edu

Authors

Weiwei Fan – Department of Nuclear Science and Engineering, Massachusetts Institute of Technology, Cambridge, Massachusetts 02139, United States; orcid.org/0000-0001-6298-8964

Baoming Wang – Department of Materials Science and Engineering, Massachusetts Institute of Technology, Cambridge, Massachusetts 02139, United States

Rui Gao – Department of Nuclear Science and Engineering, Massachusetts Institute of Technology, Cambridge, Massachusetts 02139, United States

Georgios Dimitrakopoulos – Department of Nuclear Science and Engineering, Massachusetts Institute of Technology, Cambridge, Massachusetts 02139, United States; Department of Mechanical Engineering, Massachusetts Institute of Technology, Cambridge, Massachusetts 02139, United States; orcid.org/0000-0001-6636-0517

Jiayue Wang – Department of Nuclear Science and Engineering, Massachusetts Institute of Technology, Cambridge, Massachusetts 02139, United States; orcid.org/0000-0002-2027-3634

Xianghui Xiao – National Synchrotron Light Source II, Brookhaven National Laboratory, Upton, New York 11973, United States

Lu Ma – National Synchrotron Light Source II, Brookhaven National Laboratory, Upton, New York 11973, United States

Kai Wu – State Key Laboratory of Electrical Insulation and Power Equipment, Xi'an Jiaotong University, Xi'an 710049, People's Republic of China

Complete contact information is available at: <https://pubs.acs.org/doi/10.1021/jacs.1c12970>

Notes

The authors declare no competing financial interest.

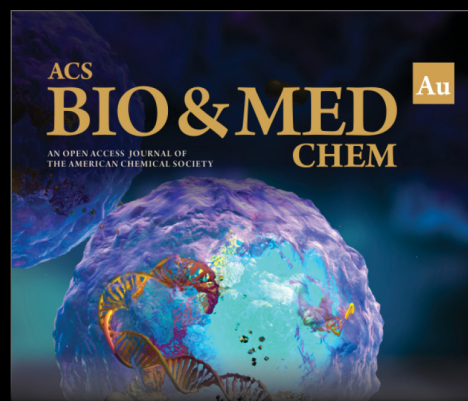
■ ACKNOWLEDGMENTS

This research used resources 7-BM and 18-ID of the National Synchrotron Light Source II, a U.S. Department of Energy (DOE) Office of Science User Facility operated for the DOE Office of Science by Brookhaven National Laboratory under Contract No. DE-SC0012704. This work was supported by LCEC MATERIALS SEED, Grant Numbers 2565243 (J.L.) and 2565244 (B.Y.). The authors thank the Materials Research Science and Engineering Center (MRSEC) facilities at MIT's Materials Research Lab (MRL), supported by the National Science Foundation (NSF) Award No. DMR-14-19807.

■ REFERENCES

- (1) Voorhoeve, R. J. H.; Johnson, D. W.; Remeika, J. P.; Gallagher, P. K. Perovskite oxides: materials science in catalysis. *Science* **1977**, *195*, 827–833.
- (2) Zhang, Y.; et al. Thermal-expansion offset for high-performance fuel cell cathodes. *Nature* **2021**, *591*, 246–251.
- (3) Tsvetkov, N.; Lu, Q. Y.; Sun, L. X.; Crumlin, E. J.; Yildiz, B. Improved chemical and electrochemical stability of perovskite oxides with less reducible cations at the surface. *Nat. Mater.* **2016**, *15*, 1010–1016.
- (4) Irvine, J. T. S.; et al. Evolution of the electrochemical interface in high-temperature fuel cells and electrolyzers. *Nat. Energy* **2016**, *1*, No. 15014.
- (5) Hua, B.; et al. Activating p-blocking centers in perovskite for efficient water splitting. *Chem* **2018**, *4*, 2902–2916.
- (6) Neagu, D.; Tsekouras, G.; Miller, D. N.; Menard, H.; Irvine, J. T. S. In situ growth of nanoparticles through control of non-stoichiometry. *Nat. Chem.* **2013**, *5*, 916–923.
- (7) Zhang, Y.; et al. Unraveling the physical chemistry and materials science of CeO₂-based nanostructures. *Chem* **2021**, *7*, 2022–2059.
- (8) Chen, Y.; et al. A robust fuel cell operated on nearly dry methane at 500 °C enabled by synergistic thermal catalysis and electrocatalysis. *Nat. Energy* **2018**, *3*, 1042–1050.
- (9) Ding, D.; Li, X. X.; Lai, S. Y.; Gerdes, K.; Liu, M. L. Enhancing SOFC cathode performance by surface modification through infiltration. *Energy Environ. Sci.* **2014**, *7*, 552–575.
- (10) Neagu, D.; et al. Nano-socketed nickel particles with enhanced coking resistance grown in situ by redox exsolution. *Nat. Commun.* **2015**, *6*, No. 8120.
- (11) Kothari, M.; et al. Platinum incorporation into titanate perovskites to deliver emergent active and stable platinum nanoparticles. *Nat. Chem.* **2021**, *13*, 677–682.
- (12) Lv, H. F.; et al. Atomic-scale insight into exsolution of CoFe alloy nanoparticles in La_{0.4}Sr_{0.6}Co_{0.2}Fe_{0.7}Mo_{0.1}O_{3-δ} with efficient CO₂ electrolysis. *Angew. Chem., Int. Ed.* **2020**, *59*, 15968–15973.
- (13) Han, H.; et al. Lattice strain-enhanced exsolution of nanoparticles in thin films. *Nat. Commun.* **2019**, *10*, No. 1471.
- (14) Dimitrakopoulos, G.; Ghoniem, A. F.; Yildiz, B. In situ catalyst exsolution on perovskite oxides for the production of CO and synthesis gas in ceramic membrane reactors. *Sustainable Energy Fuels* **2019**, *3*, 2347–2355.
- (15) Myung, J. H.; Neagu, D.; Miller, D. N.; Irvine, J. T. S. Switching on electrocatalytic activity in solid oxide cells. *Nature* **2016**, *537*, 528–531.
- (16) Kyriakou, V.; et al. Symmetrical Exsolution of Rh Nanoparticles in Solid Oxide Cells for Efficient Syngas Production from Greenhouse Gases. *ACS Catal.* **2020**, *10*, 1278–1288.
- (17) Zheng, Y.; et al. A review of high temperature co-electrolysis of H₂O and CO₂ to produce sustainable fuels using solid oxide electrolysis cells (SOECs): advanced materials and technology. *Chem. Soc. Rev.* **2017**, *46*, 1427–1463.
- (18) Fu, Q.; Mabilat, C.; Zahid, M.; Brisse, A.; Gautier, L. Syngas production via high-temperature steam/CO₂ co-electrolysis: an economic assessment. *Energy Environ. Sci.* **2010**, *3*, 1382–1397.

- (19) Kobsiriphat, W.; Madsen, B. D.; Wang, Y.; Marks, L. D.; Barnett, S. A. $\text{La}_{0.8}\text{Sr}_{0.2}\text{Cr}_{1-x}\text{Ru}_x\text{O}_{3-\delta}\text{Gd}_{0.1}\text{Ce}_{0.9}\text{O}_{1.95}$ solid oxide fuel cell anodes: Ru precipitation and electrochemical performance. *Solid State Ionics* **2009**, *180*, 257–264.
- (20) Howald, R. A. The thermodynamics of tetraenaite and awaruite: A review of the Fe-Ni phase diagram. *Metall. Mater. Trans. A – Phys. Metall. Mater. Sci.* **2003**, *34*, 1759–1769.
- (21) Sun, Y. F.; et al. A-site-deficiency facilitated in situ growth of bimetallic Ni-Fe nano-alloys: a novel coking-tolerant fuel cell anode catalyst. *Nanoscale* **2015**, *7*, 11173–11181.
- (22) Wallace, W. T.; Min, B. K.; Goodman, D. W. The nucleation, growth, and stability of oxide-supported metal clusters. *Top. Catal.* **2005**, *34*, 17–30.
- (23) Wang, J. Y.; et al. Tuning point defects by elastic strain modulates nanoparticle exsolution on perovskite oxides. *Chem. Mater.* **2021**, *33*, 5021–5034.
- (24) Kim, K. J.; et al. Facet-dependent in situ growth of nanoparticles in epitaxial thin films: the role of interfacial energy. *J. Am. Chem. Soc.* **2019**, *141*, 7509–7517.
- (25) Gao, Y.; Chen, D. J.; Saccoccio, M.; Lu, Z. H.; Ciucci, F. From material design to mechanism study: Nanoscale Ni exsolution on a highly active A-site deficient anode material for solid oxide fuel cells. *Nano Energy* **2016**, *27*, 499–508.
- (26) Katz, M. B.; et al. Self-regeneration of Pd-LaFeO_3 catalysts: new insight from atomic-resolution electron microscopy. *J. Am. Chem. Soc.* **2011**, *133*, 18090–18093.
- (27) Duan, M. Y.; et al. Reconstruction of supported metal nanoparticles in reaction conditions. *Angew. Chem., Int. Ed.* **2018**, *57*, 6464–6469.
- (28) Wahlström, E.; et al. Bonding of gold nanoclusters to oxygen vacancies on rutile TiO_2 (110). *Phys. Rev. Lett.* **2003**, *90*, No. 026101.
- (29) Oh, T. S.; et al. Evidence and model for strain-driven release of metal nanocatalysts from perovskites during exsolution. *J. Phys. Chem. Lett.* **2015**, *6*, 5106–5110.
- (30) Riess, I.; Janczkowski, H.; Nölting, J. O_2 chemical potential of nonstoichiometric ceria, CeO_{2-x} , determined by a solid electrochemical method. *J. Appl. Phys.* **1987**, *61*, 4931–4933.
- (31) Tuller, H. L.; Nowick, A. S. Defect structure and electrical properties of nonstoichiometric CeO_2 single crystals. *J. Electrochem. Soc.* **1979**, *126*, 209–217.
- (32) Kröger, F.; Vink, H. J. Relations between the concentrations of imperfections in crystalline solids. *Solid State Phys.* **1956**, *3*, 307–435.
- (33) Lin, Y. Y.; et al. Electron-induced Ti-rich surface segregation on SrTiO_3 nanoparticles. *Micron* **2015**, *68*, 152–157.
- (34) Yan, P. F.; et al. Injection of oxygen vacancies in the bulk lattice of layered cathodes. *Nat. Nanotechnol.* **2019**, *14*, 602–608.
- (35) Lee, E.; Persson, K. A. Structural and chemical evolution of the layered Li-excess Li_xMnO_3 as a function of Li content from first-principles calculations. *Adv. Energy Mater.* **2014**, *4*, No. 1400498.
- (36) Vashook, V.; et al. Potential new solid oxide fuel cell (SOFC) anode materials in the La-Ca-Cr-Ti-Ru-O system. *Fuel Cells* **2006**, *6*, 293–302.
- (37) Vashook, V.; et al. A-site deficient perovskite-type compounds in the ternary $\text{CaTiO}_3\text{-LaCrO}_3\text{-La}_{2/3}\text{TiO}_3$ system. *J. Alloys Compd.* **2006**, *419*, 271–280.



Editor-in-Chief: **Prof. Shelley D. Minteer**, University of Utah, USA



Deputy Editor
Prof. Squire J. Booker
Pennsylvania State University, USA

Open for Submissions

pubs.acs.org/biomedchemau



ACS Publications
Most Trusted. Most Cited. Most Read.